Quartz Stressing and Fracturing by Pore Pressure Dropping Down to Negative Pressure

Lionel Mercury, Emmanuel de Bilbao, Patrick Simon, Hugues Raimbourg, Isabelle Bergonzi, Claudie Hulin, Aurélien Canizarès, Kirill Shmulovich

▶ To cite this version:

Lionel Mercury, Emmanuel de Bilbao, Patrick Simon, Hugues Raimbourg, Isabelle Bergonzi, et al.. Quartz Stressing and Fracturing by Pore Pressure Dropping Down to Negative Pressure. ACS Earth and Space Chemistry, 2021, 5 (2), pp.170-185. ⟨10.1021/acsearthspacechem.0c00224⟩. ⟨insu-03130207⟩

HAL Id: insu-03130207

https://insu.hal.science/insu-03130207v1

Submitted on 3 Feb 2021

ACS EARTH AND SPACE CHEMISTRY

http://pubs.acs.org/journal/aesccq

Article

Quartz Stressing and Fracturing by Pore Pressure Dropping Down to Negative Pressure

Lionel Mercury,* Emmanuel De Bilbao, Patrick Simon, Hugues Raimbourg, Isabelle Bergonzi, Claudie Hulin, Aurélien Canizarès, and Kirill I. Shmulovich

Cite This: https://dx.doi.org/10.1021/acsearthspacechem.0c00224

Read Online

ACCESS | Metrics & More | Article Recommendations

ABSTRACT: In water-bearing porous rocks, pore pressure variations play a major role in deformation, through dissolution−precipitation and fracturing processes. An often-overlooked variation where pressure falls to negative pressure or tension can operate whenever aquifer formations dry out, for instance, in deep storage (nuclear or industrial wastes, long-term CO_2 mitigation, short-term energetic resources, etc.). This can generate capillary tension within the aquifers. This study investigates the mechanical effect of such in-pore tension in the surrounding crystal field, through laboratory experiments at the one-pore scale. Microthermometric procedures were carried out on synthetic fluid inclusions to generate large tensile stress and were combined with Raman microspectrometry to visualize the resulting stress fields in the host quartz. For comparison, we numerically modeled the stress field by linear elasticity theory. The experiments demonstrate that significant damage is produced in crystalline materials by the pore tension. Despite the induced stress measured by micro-Raman spectrometry to remain moderate, it is able to fracture the quartz. The volume of the cavity is a prominent controlling parameter for the stress amplitude. The crystalline heterogeneities of the solid are another major parameter for localizing the mean weak stress and accumulating overstress. Our results call for bringing pore-scale micromechanics into the safety assessment of the geological storage of various wastes inside depleted aquifers. They also show the magnifying effect of heterogeneities on propagating stress and localizing it along certain directions, promoting the final failure of water-bearing minerals, rocks, or pore networks.

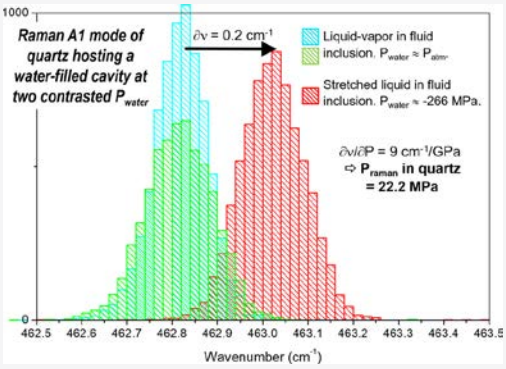

KEYWORDS: *tensile strength, pore rock damage, storage safety, Raman scattering, quartz weakening, fluid inclusions*

1. INTRODUCTION

Modern societies have growing interest in water-depleted aquifers for various storage operations, which are often accompanied by enhanced drying and increasing water tension (liquid negative pressure) in the liquid infilling the pores. Water tension in pores does induce a stress in the solid lattice around the fluid-bearing cavity, which is largely overlooked while possibly conducive to crystal failure. Even in the subcritical cracking regime, low stresses, possibly amplified at the tip of microcracks because of pre-existing flaws in the rock, and slow processes, persisting in the long term, can result in rock failure (e.g., refs.[1,2]).

The micromechanics of such situations can be treated similarly to the drying-driven damage occurring in rocks at variable humidities (e.g., refs.[3,4]). The theory involves the role of variable water saturation, of capillary bridging forces crossing the micro/nanopores, and of disjoining forces that hinder adsorption of water in nanopores, all processes that cause strain softening and microcracking. In all these studies, it is difficult to distinguish at the relevant scale the mechanical role of field stress created by pore tension from stress corrosion of chemical origin, which contributes to water weakening.[5,6] In particular, imaging and quantification of the microstress in the solid network, before and after fluid tension sets up in the pores, have been missing until now.

The challenges associated with this area of research are first in materials science in which several examples of tension-driven fracture processes still require mechanistic explanations or quantification. While sol−gel processing explains how drying-driven stress causes bodies to crack, how nanoparticle suspensions dry is much less understood, depending appreciably on molecular-scale physics combining capillary and viscous forces (e.g., refs.[7,8]). How cementitious materials dry is also of interest. There is little doubt there, ever since the pioneering work[9,10] showing that the main driving force is

Received: August 19, 2020
Revised: January 21, 2021
Accepted: January 21, 2021

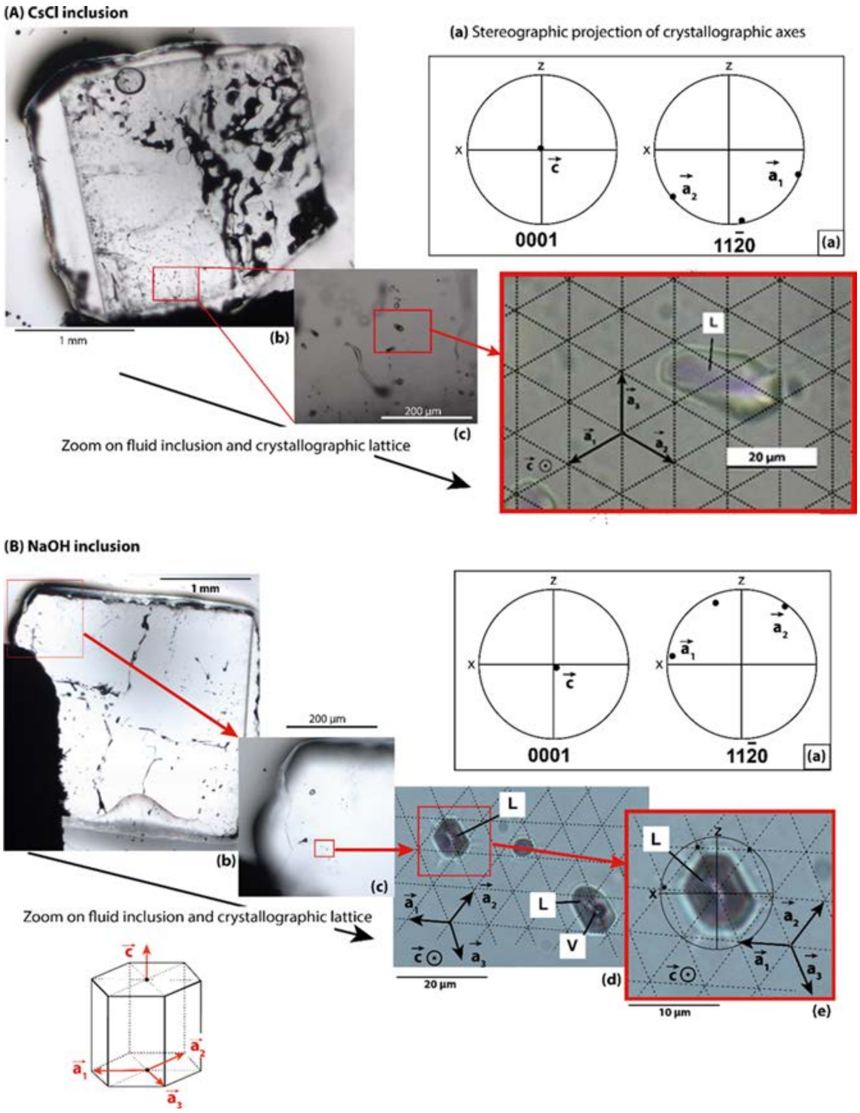

Figure 1. Photomicrographs and EBSD measurements of the two inclusions of interest (L = liquid aqueous solution; V = vapor). A. CsCl inclusion entirely filled by aqueous solution. B. NaOH inclusion. For each inclusion, two stereoplots show the orientation of the [0001] and [11$\bar{2}$0] axes within the host quartz, located perpendicular and parallel to the polishing plane, respectively. The redundant coordinate system (a_1, a_2, a_3, c) is used (hexagonal lattice).

capillary tension, possibly relayed in the smallest spaces by disjoining pressure effects (e.g., refs[11−14]). However, the main challenges are the role these processes may play in crystalline natural rocks, as for hydrosystems subjected to drying operations. The issue is understanding if and how these processes are able to generate new pore-scale stress fields and modify the cracking network of a rock as well as the air/water permeability throughout the aquifer. For illustration, nuclear waste storage in low-permeability rocks requires shaft and drift mining that dries out the rocks, expected over a few meters around galleries (e.g., refs[15−19]). On the one hand, ventilation of the tunnels promotes high tensions that can reach −100 MPa or more.[19] On the other hand, geochemical traces of air introduction are recorded up to 21 meters from the ventilated tunnel, whereas the formation is assumed to be water-saturated at such a distance (e.g., refs.[18,20]). The second illustration is the injection of (supercritical) CO_2 into deep aquifers. This provokes intense drying in the near field of the wellbore with strong and counterintuitive capillary effects.[21−23] Third, enhanced-oil recovery operations play with successive sequences of various fluid injections (air, liquid, and oil). The water invasion in dried rocks is known to induce weakening effects without a clear viewpoint on the active mechanisms (e.g., refs.[24,25]). Fourth, salt damage to cultural heritage stones is mostly interpreted as the role of crystallization pressure but is accompanied by significant desaturation and capillary effects (e.g., refs.[14,26]).

The key objective of this contribution is therefore to address drying-driven microcracking mechanisms, which may downgrade the material's quality and impact the physical properties (transmissivity and safety storage) of the damaged rock. Two experiments were designed with fluid inclusions synthesized in monocrystalline quartz and filled with aqueous solutions. As such, they stand for pores in crystalline and cemented materials but cannot be directly used to draw conclusions on natural fluid inclusions that contain less structural water and lower dislocation densities than synthetic fluid inclusions (SFIs). The occluded liquid was put under variable high tensions with various time frames, according to a microthermometric procedure (closed univariant system) (e.g., refs[27−31]). The

Raman shift of the quartz was mapped and shown to vary as a function of the in-pore tension, therefore visualizing the internal stress fields in the host crystal.

Two levels of damage occurred during the course of these experiments: optically invisible damage at the microscale and visible fracturing of the host quartz. The experimental investigations were compared to a numerical simulation based on isotropic linear elasticity. The distance of influence of the in-pore tension inside the host quartz appears strikingly larger than expectable, while the simulated and measured distributions of stress in the crystal match.

2. MATERIALS AND METHODS

2.1. Samples. SFIs have been synthetized in two monocrystalline pieces of hydrothermal quartz. After thermal fracturing, the quartz pieces were healed at high pressure and temperature (P,T) by SiO_2 overgrowth, in the presence of an aqueous solution of known composition.[30] One quartz piece was healed in the presence of a CsCl 13.6 M (69.6 wt %) brine, at 630 MPa and 480 °C for 20 days. Under ambient conditions, CsCl inclusions contain either two phases (a bubble of gas and a liquid phase) or a monophasic liquid-only phase (Figure 1). This trapped solution is known to sustain the most extreme tensile strength ever recorded in aqueous fluids[30] and therefore will serve to install super-high tensile stress. In addition, the decreasing water activity associated with the CsCl electrolyte (0.57 from Pitzer calculations at 25°C[32]) may contribute to water weakening by enhancing solubility, especially at the stress concentration zones.

The other quartz piece was hydrothermally treated at 500 °C, 600 MPa for 45 days, in the presence of a 0.2 M NaOH dilute solution. Under ambient conditions, these NaOH inclusions also contain either two phases—a bubble of gas and a liquid phase—or a monophasic liquid-only phase (Figure 1). The dilute NaOH solution trapped under high-density conditions is prone to install liquid tension at room temperature (RT)[30] and so serves to exhibit long-term tensile stress.

These two electrolytes make the quartz more soluble, especially under the synthesis conditions (0.63 GPa, 480 °C, and 20 days for the first; 0.6 GPa, 500 °C, and 45 days, for the second), so they may produce inclusions with very good inner surfaces well prone to hosting superheating processes. According to previous datasets,[30] and as mentioned above, CsCl solutions can sustain the most extreme tensile strength ever recorded in aqueous fluids, while dilute NaOH solutions are efficiently superheated at RT or below (high-density samples). Additionally, the role of both electrolytes during these experiments should have enforced the tensile stress by a chemical "weakening" effect. However, considering the slow kinetics of the dissolution−precipitation process under the thermometric cycle conditions, this effect is certainly of secondary importance.

Electron back-scattered diffraction (EBSD) was used to determine the crystallographic orientation of the quartz samples around the fluid inclusions, after the microthermometric studies, to prevent any electron-driven defects. To do so, thin sections were chemically polished with a colloidal silica suspension (0.04 μm colloidal silica suspension, Struers) and then carbon-coated to prevent charging effects. All sections were tilted by 70° to the electron beam to produce clear diffraction patterns. Data were collected using an EDAX PEGASUS EDS/EBSD system and processed with OIM DC 6.4 software (manufacturer EDAX, Mahwah, USA), available at BRGM (Orléans, France). The working distance was of about 18 mm, at an accelerating voltage of 25 kV.

The samples are platelets containing the *a*- and *b*-axes and thus perpendicular to the crystallographic c-axis (Figure 1).

2.2. Method 1: Establishing Tensile Conditions in the Pore Fluid. High tension can be produced in a liquid occluded inside a closed cavity, by making it monophasic through increasing temperature and then cooling down this monophasic liquid below the saturation curve along a constant volume trajectory. This procedure was largely used in the past to study the phase diagram of tensile water (e.g., refs.[27−31]) and the corresponding changes of phase equilibria (e.g., refs.[33,34] using fluid inclusions; refs.[35,36] using Berthelot tubes).

The starting pore material generally contains a biphasic liquid + vapor assemblage (L + V). With progressive heating, the liquid density and bubble pressure change, and the trapped liquid progressively invades the whole inclusion space (A to B path, Figure 2) up to a particular density where there is no more vapor (point B, Figure 2). The inclusion is then recognized to be homogenized at the corresponding "homogenization temperature" (T_H). Further heating drives the $P-T$ conditions in the inclusion along the isochore curve inside the stable domain of liquid (B to C path, Figure 2). The second step is the progressive cooling of the sample, which follows the isochoric path as long as the inclusion remains homogeneously filled with liquid (C to D path without nucleation at B, Figure 2). Once T_H is crossed without bubble nucleation, the monophasic liquid becomes metastable; that is, it is less stable than the liquid−vapor assemblage. The nucleation does not occur as long as the energy cost of the vapor−liquid interface fabrication is higher than the gain afforded by the bulk energy of the most stable phase.[31,38] Such a monophasic liquid is superheated (located to the right of the saturation curve) and follows an isochoric cooling down to a certain temperature at which a bubble appears suddenly. This is the instantaneous nucleation temperature (T_{IN}), which is always located within the tensile domain: nucleation in fluid inclusions disobeys the saturation conditions. After nucleation, the newly formed LV assemblage moves instantaneously back to the saturation curve conditions (D to E path, Figure 2). This

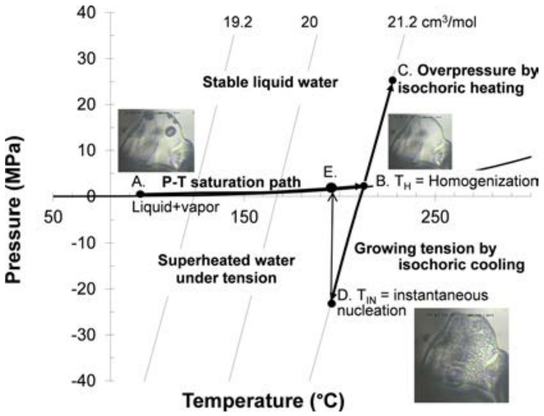

Figure 2. Phase diagram of pure water in the P−T space, calculated with the IAPWS-95 equation of state.[37] Each isochore is labeled with the molar volume in $cm^3 \cdot mol^{-1}$. The CsCl inclusion micrographs illustrate the fluid content present in the cavity at each characteristic step.

procedure fabricates tensile water similar to that retrieved at the high capillary degree that forms under drying conditions.

All thermal sequences were carried out on a Linkam heating−cooling stage THMS600, at a slow rate (2 °C/min) to avoid any temperature overshoot and guarantee a thermal equilibrium at each set point.

2.3. Method 2: Measuring the Stress in the Container.

In situ Raman spectrometry can be used to record the temperature/pressure shift of a solid material because of the anharmonicity of a Raman-active vibration mode.[39] Anharmonicity is generally considered to have two contributions: explicit ones (as phonon−phonon interactions) and implicit ones coming from changes in bond lengths (under P or T variations) (e.g., refs.[40,41]). Both will lead to the wavenumber shift of vibration modes upon external solicitations such as temperature or hydrostatic pressure. A previous study on quartz[42] investigated the changes in wavenumber and linewidth of the 206 and 464 cm^{-1} A_1 Raman modes of SiO_2 from 23 to 800 °C and from 0.1 MPa to 2.1 GPa. It was observed that, under hydrostatic stress, the wavenumber shift of the 464 cm^{-1} peak at RT (23 °C) depends linearly on pressure up to 0.5 GPa: $d/dP = 8.7$ cm^{-1}/GPa. The wavenumber shift for the 206 cm^{-1} mode also has linear pressure dependency, twice as much at $\text{d}/\text{d}P = 20$ cm^{-1}/GPa. Schmidt and Ziemann[42] considered an isotropic stress according to the Grüneisen formalism, with a linear dependence between stress and Raman wavenumber. This linear approach is certainly the most reliable to treat the complex case of a noncubic crystalline symmetry, noninfinite crystal because of the inclusion vicinity, and nonuniform force field and is the method used here, assuming that the stress field induced by pressure change in the fluid inclusion is similar to hydrostatic stress and considering the isotropy in (a,b)-plane. As no resonant Raman scattering effect occurs here, the stress/Raman shift relation obtained by Schmidt and Ziemann[42] with a 514.5 nm laser can be used for any other nonresonant Raman excitation laser line.

The measurements were performed on a Renishaw inVia Reflex spectrometer, using the 633 nm excitation line of a He−Ne laser (less than 10 mW on the sample). The grating was 1800 grooves/mm, giving a wavenumber step between two adjacent pixels of the charge-coupled device equal to 0.97 cm^{-1}. Each mapping measurement was performed after a wavenumber calibration procedure of the spectrometer on its internal silicon reference sample (520.5 cm^{-1}), without moving the quartz sample, which ensures the calibration state and promotes the best possible reproducibility. The calibration was systematically checked after map acquisitions and was stable within an accuracy much better than ±0.1 cm^{-1} over 24 h (no detectable change of the 520.5 cm^{-1} position). The microscope (DM2500 Leica) lens compatible with this configuration was a Leica 50X long front distance (NA = 0.50). Each individual Raman spectrum was obtained with an accumulation time of 10 s. Because of the small diameter of the Raman spot (≈ 2 μm) and the size of the inclusions, maps of around 7600 points were acquired, with an acquisition total time reaching 20 h. The map acquisitions were performed in the Renishaw StreamlineHR mode, optimizing the acquisition time and the vertical resolution (equivalent to a confocal mode), here estimated to be better than 2 μm.

Spectra were treated with Renishaw Wire 3 software. The Raman spectra were not baseline-corrected but directly fitted with a Gauss−Lorentz (G/L hereafter) profile, to involve even the tiniest distortions in the analysis. Very small differences between mono- and biphasic conditions could thus be probed because the spectra were acquired with strictly identical conditions (optical configuration and temperature), apart from the pressure inside the inclusion. No Bose−Einstein thermal correction was performed[43] because Raman shifts were compared at identical temperatures under two different pressure conditions (monophasic and biphasic regimes).[39]

2.4. Method 3: Super-Stressing the Container toward Failure.

Two methods were used to establish whether the stress induced in quartz by the in-pore tension was able to provoke the quartz failure. First, the characteristics of the CsCl fluid inclusion allowed us to subject it to high tension cyclically. The procedure was simply to put the inclusion at various temperatures of measurements (T_{MEAS}) corresponding to different high tensions and leave the inclusion in this monophasic metastable state until cavitation occurs, bringing back the inclusion to the LV equilibrium state. Then, the inclusion was homogenized and again cooled down to a certain T_{MEAS} pursuing the cycle. From a mechanical point of view, these repeated stress conditions can damage the solid depending on the lattice's defaults, the intensity of the stress, and the number of cycles.

Second, the NaOH fluid inclusions allowed us to install high-tension conditions at RT, so the liquid tension could be readily maintained over a long time. Therefore, stress is accumulated within the sample over time, as long as bubbles are absent (easily verified by optical observations) in the superheated inclusions: this was a permanent or "enduring" tension experiment, corresponding to purely static stress conditions.

2.5. Method 4: Simulating the Stress in the Host Crystal as a Function of in-Pore Fluid Tension.

Numerical simulations of the experiments were performed by finite element analysis (FEA hereafter) using Comsol Multiphysics software for a deeper understanding of the stress change observed by Raman spectroscopy. In the first approach, the sample was modeled as a 2D axisymmetric solid containing an oblate spheroidal inclusion.[44] The stress field around a cavity has been studied many times. In particular, Eshelby[45] studied how an applied stress, uniform at large distances, is disturbed by a cavity. From this early work, many analytical or closed-form analytical solutions have been proposed for spherical or spheroidal inclusions and considering isotropic or anisotropic materials.[46−54] The problem becomes more complicated for a spheroidal cavity hosted in an anisotropic solid. On the other hand, FEA has proved its reliability for solving mechanical problems especially in the case of linear elastic problems but also in the case of geometric nonlinearity and with nonlinear isotropic elastic materials.[55] Actually, FEA can be applied whatever the geometry of the inclusion.

In a first approach, the sample was modeled as a 2D axisymmetric solid containing an oblate spheroidal inclusion,[44] and the finite-element-based results were compared with theoretical results obtained using the code recently developed by Meng et al.[51−53] which gives quasianalytical strain/stress fields following Eshelby's solution, with the elliptic integral approximated through a numerical routine. The purpose of this comparison was to determine the size of the solid surrounding the cavity to avoid boundary effects and define the meshing strategy to avoid numerical artifacts or errors and to better understand the stress field building around the inclusion. An isotropic elastic material was defined in the solid part with Young's modulus of 100 GPa and Poisson's coefficient of

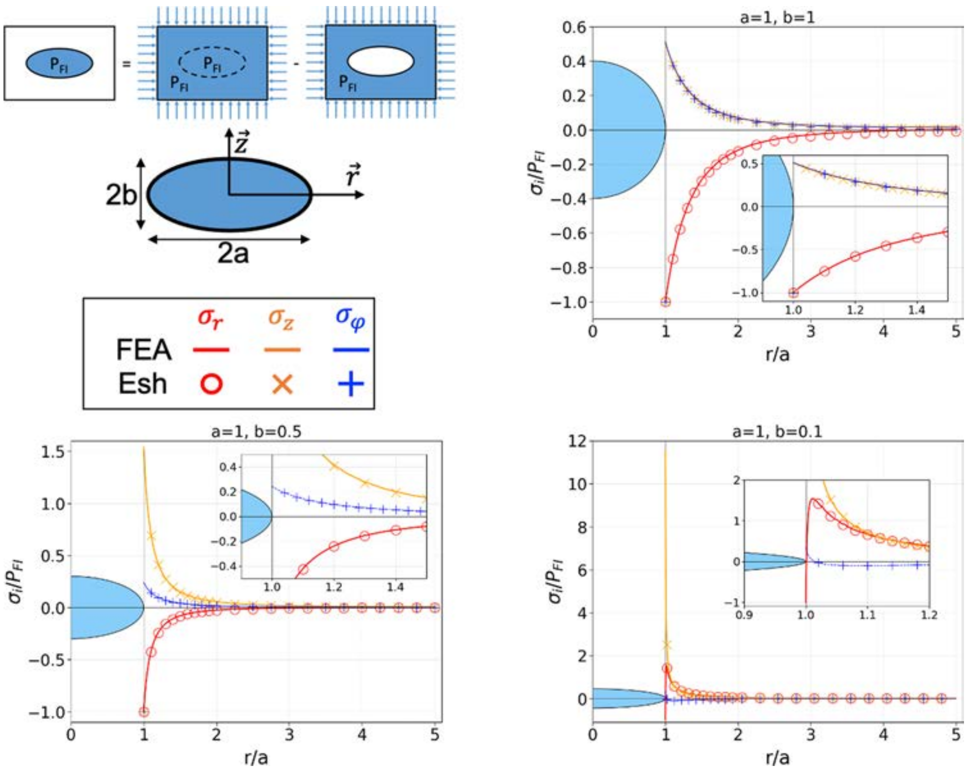

Figure 3. Normalized stress along the radial axis. The normalized stresses are calculated by dividing the stresses by the pressure applied onto the inclusion wall. The normalized radial coordinate is the radial coordinate divided by the half-length of the spheroid, $r^* = r/a$. The stresses denoted "Esh" were calculated following Eshelby's theory[45] by applying script developed by Meng et al.[51−53] and according to the superposition principle for linear elastic mechanics (top-left of the figure). Stresses that were noted by FEA were calculated using Comsol Multiphysics software. For all the calculations, Young's modulus and Poisson's coefficient were 100 GPa and 0.06, respectively, according to ref.[56]

0.06.[56] These elastic properties correspond to equivalent quasi-isotropic quartz obtained by Voigt−Reuss−Hill averaging.[56] The inclusion was defined with null elastic constants, and a negative pressure P_{FI} (e.g., $P_{FI} = -1$ MPa) was applied on the cavity wall. For the theoretical solution, the superposition principle was applied as the code because it does not directly apply pressure on the cavity wall (Figure 3, top, left). Unstructured triangular quadratic elements were applied for the FEA, and zero displacement was applied to the symmetry plane (horizontal) perpendicular to the revolution axis (vertical). The stresses σ_{ii}/P_{FI} lying along the radial direction were compared (Figure 3). For the sake of simplicity, the stress sign convention commonly used in mechanics has been changed in this paper, and a positive stress refers to a compressive state. The pressure has also been changed $P_T = Tr(\overline{\overline{\sigma}})/3$ instead of $P_T = -Tr(\overline{\overline{\sigma}})/3$ to keep its usual meaning, namely, a positive value refers to a compressive state. The stresses were normalized by dividing each of them by P_{FI} ($\sigma_{ii}{}^*=\sigma_{ii}/P_{FI}$), and the radial coordinate was divided by the half-length of the ellipse a ($r^* = r/a$).

We considered three shapes defined by the semiaxis ratio b/a (hereafter called shape factor), where a and b are the semiaxes in the radial and axial directions, respectively. The third semiaxis c is equal to the radial axis in the oblate spheroid. Simulated results are in very good agreement with theoretical results for all the stresses, proving that the solid model size was large enough and the meshing strategy was suitable. The FEA model was validated. The results show clearly the stress concentration effect induced by the cavity and the dependence of the concentration amplitude on the shape factor b/a. For a sphere, $b/a = 1$, the axial and tangent stresses are equal and compensate the radial stress, and the resulting pressure is null. Each stress does not exceed the pressure, and no stress concentration effect occurs. On the contrary, when the spheroid is flattened, the axial and tangent stresses are not equal any longer, and they do not compensate the radial stress. The axial stress largely predominates the other stresses and reaches up to 12 times the fluid inclusion pressure. The positive values of the axial stress and pressure indicate a compressive state in equatorial plane although a tensile stress is applied on the cavity wall (negative pressure PFI) (Figure 4). This effect is due to the flattening of the spheroid and is magnified when the shape factor decreases.

Once validated, the ellipsoid-based model was used to simulate the experiments. A negative (tensile) pressure was applied on the 2D elliptical edge to simulate the in-pore pressure change. No gradient or interfacial effects of any sort that may "buffer" the liquid-to-solid pressure transmission were taken into account. The anisotropy of α-quartz was considered, and the elastic moduli were defined according to Calderon et al.[57]

Second, the sample was modeled with a 3D prismatic solid containing a faceted inclusion to look like the inclusion observed with Raman spectroscopy (Figure 5). Only an eighth of the sample was modeled considering symmetry conditions, and the dimensions were defined to match the inclusion actually considered. Zero displacement was applied to the three symmetry planes (SP), and a negative pressure was again applied on the inner surfaces of the inclusion. The same

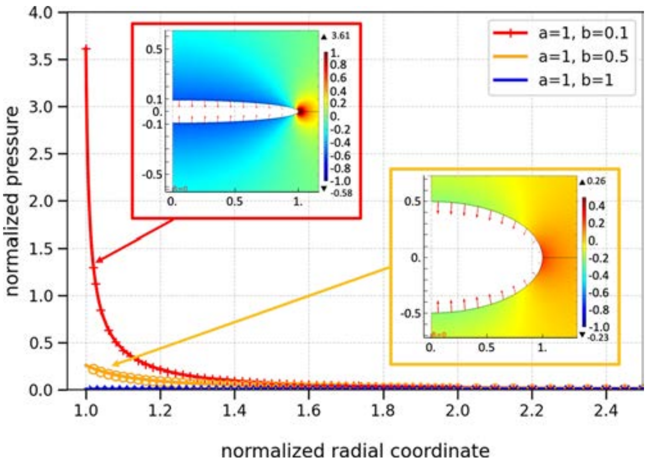

Figure 4. Simulation of a host with a spherical or spheroidal inclusion with a negative (tensile) pressure applied on the wall cavity. See Figure 1 for more details on the model. Normalized pressure simulated with FEA and depending on shape factor b/a, maps, and values along the radial axis. For each shape factor, the continuous line and marks represent the FEA-based pressure and the Eshelby-based pressure, respectively.

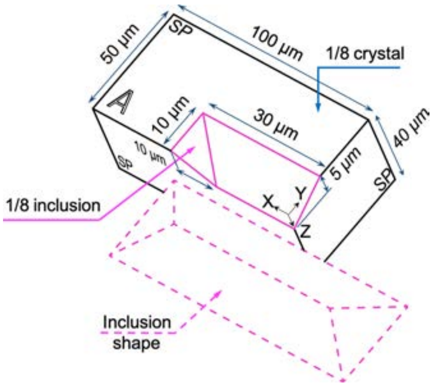

Figure 5. Geometry of the 3D mechanical model of the inclusion for the FEA. Because of symmetries (SP), only an eighth of the solid is modeled. The image size is not scaled with the prism size for visibility purposes.

anisotropic elastic moduli as for the previous simulation were used.

3. EXPERIMENTAL RESULTS AND INTERPRETATION

3.1. Stressing the Container (CsCl Inclusion). The CsCl fluid inclusion has a T_H of 205.6 ± 0.4 °C and T_{IN} of 89 ± 1.4 °C. Drawing a straight line from the synthesis conditions (630 MPa and 480 °C) to the (T_H,P_H) pair ($\mathrm{d}P/\mathrm{d}T = 2.3$ MPa/°C), and extrapolating this line to the T_{IN} value, gives the liquid tension existing in the inclusion just before the nucleation, at −266 ± 3 MPa (Figure 6).

First, the Raman maps all around a CsCl inclusion were recorded at 120 °C while the internal pressure in the liquid was either 0.12 MPa, corresponding to biphasic liquid−vapor assemblage, or − 194 MPa, corresponding to the metastable monophasic state with liquid under tension. Each mapping took 20 h. The chosen temperature of 120 °C was sufficiently above the T_{IN} to avoid any nucleation during the Raman measurement time. Indeed, the metastable lifetime depends exponentially upon the distance to T_{IN}.[58−60]

Two A_1 Raman modes of SiO_2 with highest wavenumbers were studied: the mode at 464 cm^{-1} and the mode at 206 cm^{-1}. The signal was mapped in the quartz around the inclusion (width 70 μm × height 110 μm) that contained the fluid. A G/L profile was fitted with the recorded spectrum at each point, and the characteristic wavenumber of the G/L profile was used to build the map. The map obtained with the 464 cm^{-1} mode in the stable state (biphasic liquid−vapor assemblage) shows actual wavenumbers ranging from 462.5 to 463.1 cm^{-1} with a mean value of 462.8 cm^{-1} (Figure 7). Black spots correspond to regions where the Raman line intensity decreases below a threshold and were used to locate the inclusions. The barycenter of the black spot corresponding to the inclusion of interest was used as the origin of the map. Finally, a micrograph of the inclusion of interest has been superimposed by aligning the lattice directions determined with EBSD with the Raman map with a perfect match. The dark spot is slightly bigger than the inclusion image because of the empirical determination of the threshold.

Applying the Schmidt and Ziemann[42] relation at 120 °C gives an expected wavenumber of 462.4 cm^{-1}, which can favorably be compared with our mean measured wavenumber 462.8 cm^{-1}. Because of uncertainties (absolute calibration of two different spectrometers, accuracy on the wavenumber of a "reference" quartz totally stress-free at RT), these values look similar. Though the wavenumbers of the map seem to follow a rather narrow spread, their spatial distribution is well organized around the inclusion. Four zones aligned with the crystal axes show a remarkable symmetry (Figure 7, left). In the upper and lower triangular zones (where green predominates), the wavenumber is close to 462.75 cm^{-1} while it is close to 463 cm^{-1} in the lateral zones (orange/red pixels). The sharp variation in internal pressure between these domains leads us to think of some localized strains on planar defects, presumably connected with how the inclusion formed (thermal fracturing followed by SiO_2 overgrowth).

The map obtained from inclusion in the monophasic state for the same A_1 Raman mode is presented in Figure 7 on the right. Again, the micrograph of the inclusion of interest has been superimposed. In this figure, the dark spot is hidden by the inclusion image, indicating that the dark spot is smaller than that of the biphasic state map. That is also the case for the other spot located at the bottom-right of each map. This shows that the confocal z plane slightly changed. The mean wavenumber is 463.0 cm^{-1}, ranging from 462.8 to 463.3 cm^{-1}. Again, the temperature-corrected wavenumber calculated with the Schmidt and Ziemann[42] relationship compares favorably with the "monophasic" average value. However, it is the gap between the "biphasic" and "monophasic" values which is of special interest. It is very small (0.25 cm^{-1} between 462.75 and 463 cm^{-1}), but both measurements were performed on the same spectrometer with the same calibration procedure, and on the same points of one quartz sample. Only the spectrometer stability is involved here. It is worth noting that the color scale for the monophasic state map slightly differs from the LV state one. The color scale of each map has been chosen to emphasize the similarities between the spatial distributions of the colors and consequently of the wavenumbers. Globally, the increase of the Raman wavenumbers of the monophasic state map indicates the development of compressive stress although no optical evidence of quartz failure was recorded during this experiment, which therefore follows a purely elastic behavior.

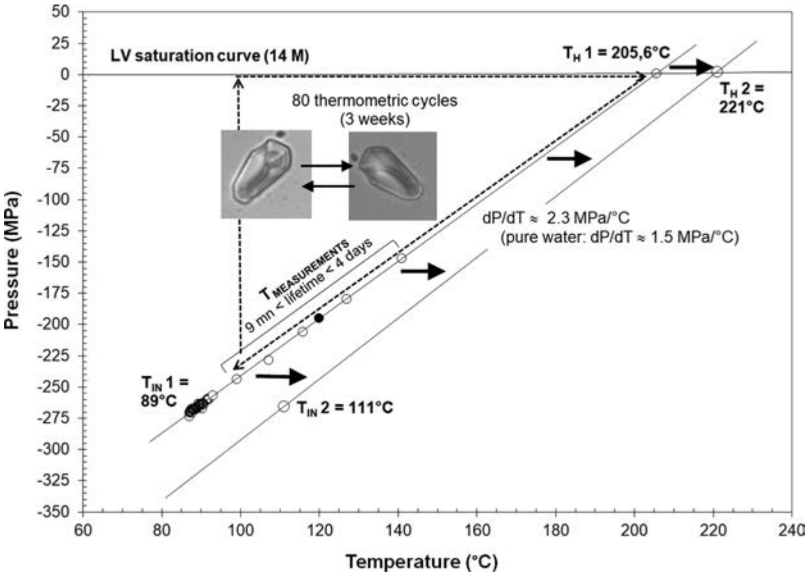

Figure 6. Thermal procedure, microthermometric features, and schematics of the cyclic tension applied to the sample, before (label 1, Section 3.1) and after (label 2, Section 3.2) the stretching irreversible failure of the inclusion.

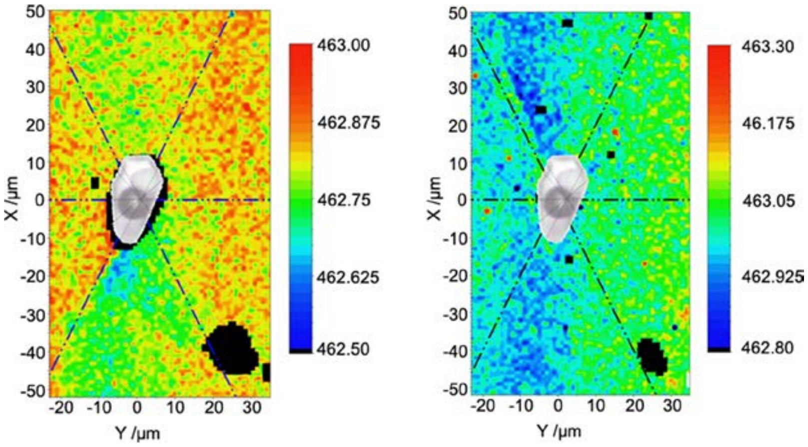

Figure 7. Raman map of the wavenumber of the high wavenumber A_1 quartz mode, with infilling fluid at the liquid−vapor saturation state (left) and monophasic liquid state (right). The wavenumber values are given by the color scale. The inclusion of interest has been superimposed as well as the crystal axes determined with EBSD.

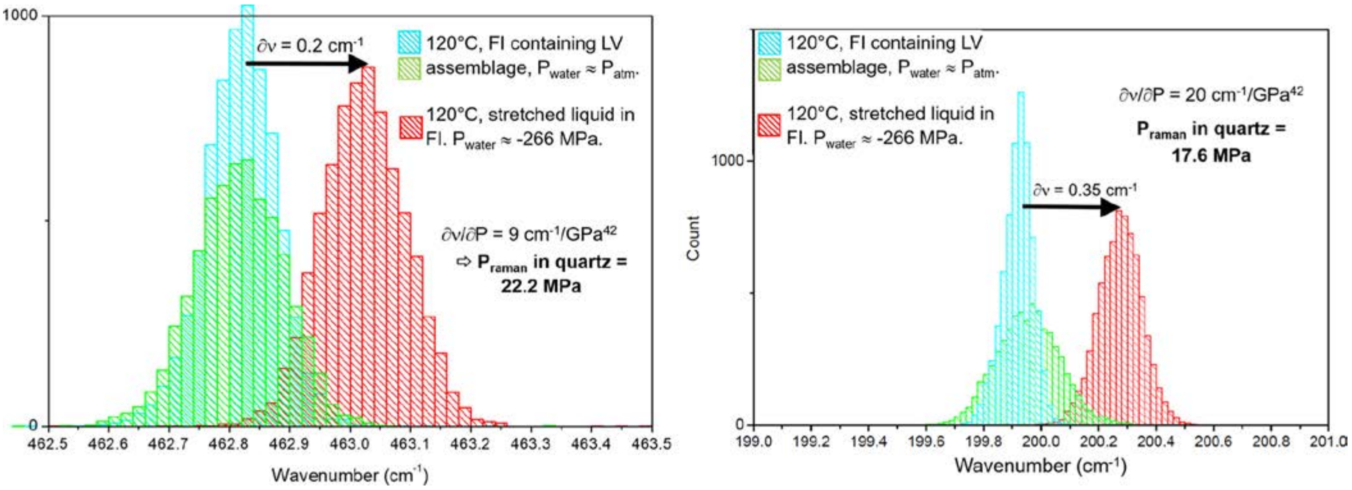

Figure 8. Raman line center histograms at 120 °C of the 464 (left) and 206 (right) cm^{-1} bands of quartz around a fluid inclusion filled with either a biphasic liquid−vapor stable mixture (green, blue = repetition to test for reproducibility) or a monophasic tensile liquid (red).

To extract the mean Raman shift provoked by the in-pore tension in the actual sample over the experimental area, the whole data set collected with each map was redrawn as the histogram of the number of occurrences in each wavenumber range, for the two Raman mode maps (464 and 206 cm^{-1}) under the two stressed conditions (Figure 8). This shows how the wavenumbers measured vary within the experimental area for the two Raman modes and also shows how regular the datasets are.

The liquid−vapor series gives the Raman modes at saturation pressure: the Gaussian maxima are at 462.8 and 199.9 cm^{-1}. These measurements were double-checked to test the reproducibility of the recorded values (blue and green histograms), and both datasets match well. The match is strictly perfect for the high wavenumber mode (same main wavenumber and same width) while the low wavenumber A_1 mode gave a 0.015 cm^{-1} change for wavenumber (showing the high stability of the experiment) with the total width varying by a maximum of 0.1 cm^{-1}. The main information we take from these graphs is the Raman gap that exists between the two 120 °C datasets at different pressures. Each mode (464 and 206 cm^{-1}) has a specific gap, quite moderate with respect to the precision of the spectrometer, but largely beyond any instrumental effect. Note that here the key factor of the spectrometer is its stability, not its spectral resolution. Specific care was taken to improve stability by avoiding thermal fluctuations and then any human presence in the experimental room. Now, using the calibration of the Raman shift with pressure,[42] it is possible to estimate the level of strain involved. The two modes agreed remarkably well for the resulting stress: 20 MPa ± 2.5 MPa (Figure 8). The small difference between the values (22.2 MPa for 464 cm^{-1} mode and 17.6 for 206 cm^{-1} mode) can be related to the wavenumber measurement uncertainty, and by the application of only one parameter on a noncubic structure, which is, moreover, not subjected to a hydrostatic pressure but to a complex stress field.

The Raman shift difference of the 464 cm^{-1} mode between the biphasic and monophasic modes was plotted as a map (Figure 9). This plot is a spatial representation of the Raman wavenumber change, that is to say the stress distribution induced by the in-pore pressure change. The difference is positive or zero, except for very rare occurrences. In addition, the average wavenumber shift and standard deviation were evaluated in four zones surrounding the inclusion. The area above the inclusion in the map is called "North," and so on. The statistics are very close in the three zones West, North, and East (see Figure 9) with a mean wavenumber shift $\delta_{\Delta\nu}^{\mathrm{av}}$ close to the 0.2 cm^{-1} overall shift (Figure 8) and a very constant standard deviation. This proves that the stress field produced by the in-pore pressure change is superimposed on an initial spatial stress/strain distribution observable in the Raman map under LV conditions (Figure 7, left). The southern zone shows a different behavior with a higher Raman shift difference (0.249 cm^{-1}) corresponding to a Raman pressure of 28 MPa. It is worth noting that the highest shift difference represented by the red/orange pixels in Figure 9 follows the crystallographic axis.

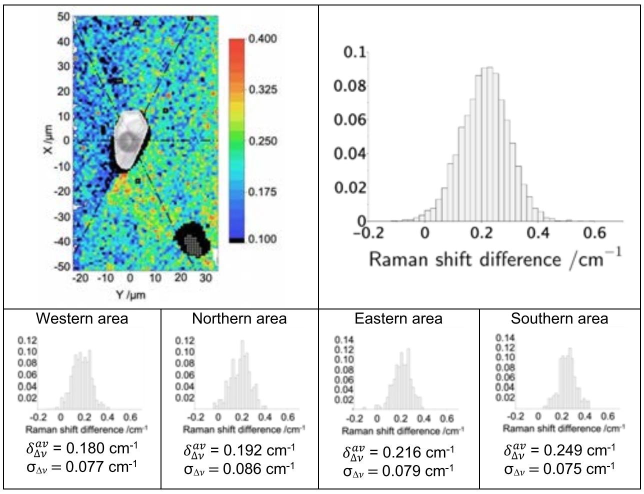

Figure 9. Shift difference between biphasic and monophasic modes for the 464 cm^{-1} Raman mode. Top-left: Map of the shift difference. Top-right: global histogram of this map. Bottom: Histograms of the four regions indicated by the red rectangles on the map, with a geographic-like denomination.

3.2. Nonvisible Failure of the Container (CsCl Inclusion).

The experiment was carried out repeatedly (see Section 2.4 with the cyclical procedure). After around 80 cycles carried out over 3 weeks, with tension lasting from some minutes to some days during each cycle, a brutal change of T_{H} was observed, expressing an internal failure (usually called "inclusion stretching" in the inclusionist's glossary; see ref.[61] for a review about the different types of damage in inclusions) and a change of the cavity volume. T_{H} was then upshifted by 16 °C, and logically, the T_{IN} changed by a similar value, at T_{IN} = 111 °C (Figure 6). Despite this thermometric evidence, the change in the cavity shape or volume was so small that it could not be observed optically (this is usual with this "inclusion stretching"), leading us to infer that the volume change resulted from the formation of damage at the microscale as a network around the inclusion, below the optical limit.

The Raman maps were then measured at 140 °C, that is to say, for the same $T - T_{\mathrm{IN}}$ difference as for the previous data sets. They showed a very weak Raman shift between the biphasic and the monophasic situations (Figure 10), much weaker than in the precracked state (Figure 8). This fact matches very well with the presence of a dense network of microcracks, diminishing the lattice stress detectable with Raman spectroscopy.

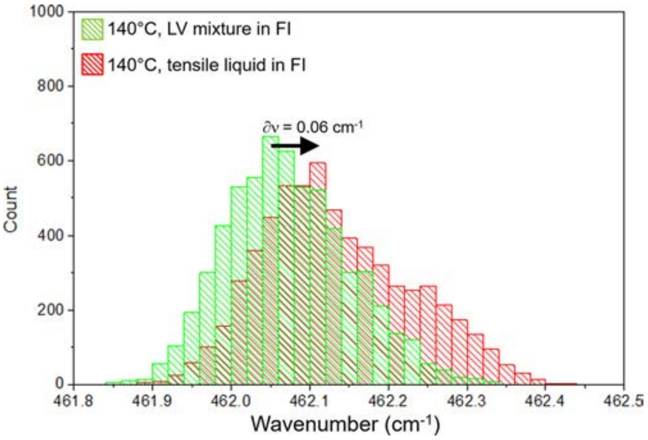

Figure 10. Histograms of the line center of the high wavenumber band, at 140 °C, along the equatorial plane of the inclusion, after the T_{H}-recorded damage.

It means that, despite the low stress thus registered, the cyclical procedure led to a real damage all around the cavity materialized by a brutal increase of T_H. The local damage is also evidenced by the Raman maps recorded after the damage of the inclusion, which show much lower values of the peak stress (i.e., for the largest tension in the inclusion), +6.7 MPa (Figure 10), compared to the precracked state (+20 MPa in the plane, Figure 8). This large drop of the in-plane stress is interpreted as the presence of a dense network of microcracks, able to adjust the liquid tensile stress by a multitude of microdisplacements inside the crack, instead of provoking a lattice stress detectable with Raman spectroscopy.

3.3. Fracturing the Container (NaOH Inclusion). The NaOH sample contains four inclusions shaped as "negative quartz crystals" (Figure 11), numbered 1 to 4. T_H is revolving around 140 °C, corresponding to a mean water density of $D \approx 926$ kg/m^3 according to IAPWS EoS (pure water approximation[37]) (Figure 11). Inclusions 1−3 did not show any instantaneous nucleation in the positive (Celsius) temperature area. At RT and after isochoric cooling from T_H, the liquid tension in the three monophasic inclusions 1−3 was −132 MPa (Figure 11). Inclusion 4 had T_{IN} equal to 44 °C so this inclusion was never under tension under ambient conditions while the three others were, giving us a "reference" inclusion without a fluid pressure effect on the nearby surroundings.

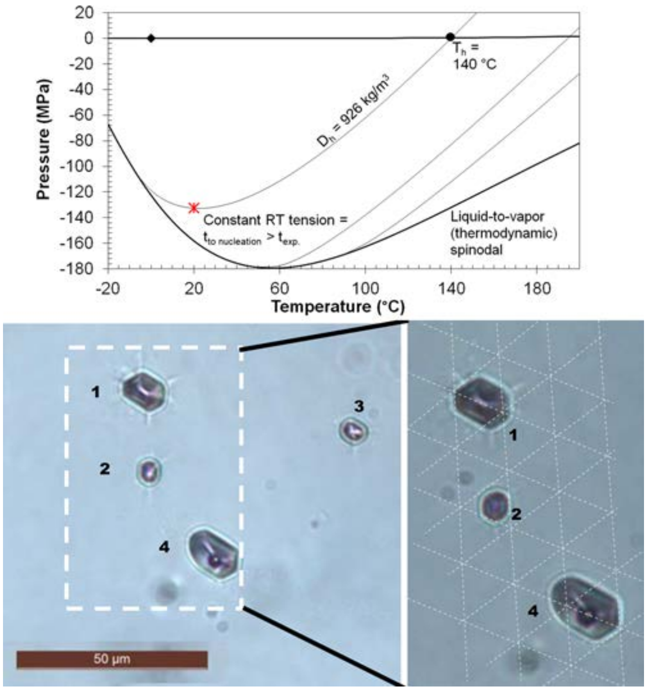

Figure 11. Upper panel, installing the "enduring tension" situation by isochoric cooling of a high-density SFI. Bottom left, observation of three fluid inclusions numbered (1−3) with microcracking in the quartz at each corner of the negatively shaped cavity. The fourth (num. 4), which does not tolerate tensile stress (see the bubble), is intact. Bottom-right, crystallographic axes measured by EBSD are reported on the right micrograph.

With this RT superheating installed in inclusions 1−3, we started observing the inclusions subjected to a permanent tension from the in-pore liquid. Surprisingly, after only some weeks and before any Raman records or accumulation of data on the inclusions of interest, the host quartz cracked all around the three inclusions hosting tensile liquid, consistent with the crystallographic axis (Figure 11, bottom-right panel).

The quartz failure occurred with optically visible cracks appearing at the edge of the three inclusions 1−3. The bright border is underlined by a similar black edge when zooming: the cracks cannot be due to an optical artifact. Inclusion 4, which was never subjected to long tension (T_{IN} > RT), was not damaged. The coexistence between the two mechanical behaviors, so well correlated with the microthermometric features, is a clear indication that the liquid tension is able to fracture the surrounding quartz.

3.4. Numerical Models of Stress Concentration and Fracturing. *3.4.1. Ellipsoidal Model and Pressure in the Equatorial Plane.* The simulated stresses and pressure resulting from FEA simulation based on oblate spheroids with a shape factor $b/a = 0.1$ are represented in Figure 12. The pressure is highly concentrated close to the inclusion edge where it reaches four times the fluid inclusion pressure and decreases sharply along the radial axis. The pressure distribution corroborates the Raman observations (Figure 10): a compressive stress (positive) lies within the equatorial plane around the cavity (red color). This can be explained by the flattening of the spheroid, like what occurred with the remote stress above. The simulation indicates that the principal stresses are aligned with the geometrical axes, that is, the radial, tangent, and axial directions of the ellipsoid (see the r, t, and z directions, respectively, in the inset top-right in Figure 12). In the equatorial plane, the compressive axial stress □$_z$ is the largest contribution to the total pressure while the magnitudes of the tangent and radial stresses □$_t$ and □$_r$ are much smaller. The tangent stress σ_t is compressive as well and contributes to a lesser extent to the total pressure. On the other hand, radial stress σ_r does not have a monotonous change. It has a negative value in the very vicinity of the edge, quickly inhibited by the global flattening of the inclusion yielding a compressive stress.

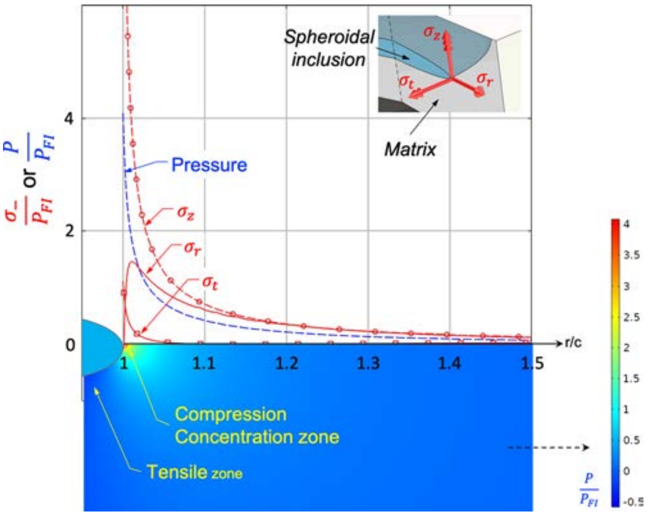

Figure 12. 2D axisymmetric mechanics model of an ellipsoidal-shaped inclusion. Bottom: Normalized pressure map around an inclusion. The vertical symmetry axis is the revolution axis. Top: Stresses and pressure magnitude along the radial axis in the optical plane.

3.4.2. Real Inclusion Shape and the Stress Concentration in the CsCl Inclusion. The Raman shift can be evaluated from either from Grüneisen's constant as shown above or from the deformation phonon potentials, usually noted p, q, and r, which are the components of the fourth rank tensor relating the changes of the spring constants of the lattice and the deformation tensor.[62] They generally are determined from hydrostatic pressure Raman experiments using diamond anvil cells, uniaxial stress experiments, or strained thin film grown by strained-layer epitaxy. It is worth noting that the third potential r relates the shear strain components of the tensor. Briggs and Ramdas[63] determined the deformation potential constants of the zone-center optical phonons of α-quartz under uniaxial stress experiments. Finally, the Raman shift can also be evaluated from the stresses using the components of the fourth rank elastic tensor relating stress and strain.

In the present case, the radial, tangent, and axial stresses are also the principal stresses because of the symmetry of the geometry and the loading, and it is therefore possible to derive the expected Raman shift from either the principal stresses or the radial, tangent, and axial stresses. Here, the constants determined by Briggs and Ramdas[63] were used to calculate the 464 cm^{-1} Raman shift from the stresses considering that the z-axis of the model coincides with the crystallographic c-axis as shown in Section 2.1:

$$\delta\nu_{A_{1,464\mathrm{cm}^{-1}}} = 0.21 \bullet 10^{-2} \times (\sigma_t + \sigma_r) + 0.38 \bullet 10^{-2} \times \sigma_z$$

where the stresses are in MPa and $\delta\nu$ in cm^{-1}. The Briggs' potentials were determined with an uncertainty of $\pm 0.02 \bullet 10^{-2}$ cm^{-1}/MPa. Note that they are here positive because of the change in the sign of the stresses. The uncertainty of the Raman shift evaluated from uncertainty propagation depends on the stresses and reaches a maximum value of 0.5 cm^{-1}.

The Raman shift was also calculated following the Grüneisen formalism:

$$\delta\nu_{A_{1,464\mathrm{cm}^{-1}}} = 8.7 \bullet 10^{-3} \times P$$

where P is in MPa and $\delta\nu$ in cm^{-1}.

Both Raman shifts were evaluated along with the radial axis (Figure 13). The very good agreement between Briggs and Grüneisen formalisms confirms that the Grüneisen's constant-based approach was really reliable in this study, as proposed in Section 2.3.

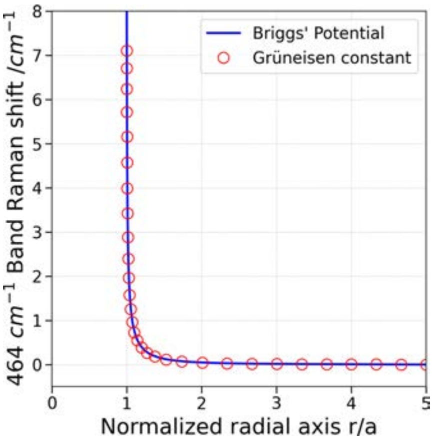

Figure 13. Raman shift evaluation along the radial axis.

Focusing on the inclusion described in Section 3.1, the Raman pressure at the bottom-right corner of the inclusion (Figure 9) was compared with the simulation of the oblate cavity with a shape factor b/a = 0.1 and anisotropic properties (Figure 14). The simulated pressure (blue line FEA) quickly tends asymptotically to zero upon moving away from the inclusion, as expected from a direct application of the theory of solid mechanics. In the meantime, the experimental values showed that the sample is under stress over the total area (red stars, Figure 14; see also the green and blue pixels, Figure 9). The pressure derived from the Raman measures shows a slight decrease, especially close to the inclusion (gray area), where the values are in the same order of the simulation. Considering the difficulty in localizing the edge of the Raman map and the assumptions for the Raman pressure calculation and the simplified geometry for the simulation and despite the dispersion of the measured values, measurements and simulation can be estimated as consistent at least from a qualitative point of view. However, the Raman pressure seems to remain constant around 25 MPa when looking over the whole map even farther from the inclusion. This asymptotic mean pressure is not at all expectable and constitutes one of the main surprises of this experimental study. Although we do not have explanations for this bias, it may be compared with the Raman gap averaged over the whole map (0.212 cm^{-1}, i.e., 24 MPa). Another point to be considered is the presence of another cavity, which might not be alone, close to the studied inclusion. The stress fields induced by these surrounding cavities might produce such a general overstress. Finally, the general overstress may also be related to the localized strain/stress induced by the inclusion synthesis procedure.

The Raman pressure appears to be a good probe of the stress fields around the water-bearing cavity, and a highly resolved measurement of the instantaneous/local stress is certainly possible according to our preliminary results. It is also clear that any change in the in-pore pressure drives a significant modification in the poromechanical stress field, over an unexpected long-range scope. To address these findings, further studies should involve the anisotropic strain propagation in the matrix along preferential axes (crystallography, dislocations, etc.) by carefully plotting how the quartz band varies from place to place, at saturation pressure. It was already clear (Figure 7 left) that our hydrothermal monocrystalline quartz was not uniform in terms of Raman shift.

3.4.3. Real Inclusion Shape and the Fracturing of the NaOH Inclusion. The objective of the FEA simulation performed on the 3D faceted cavity (Figure 5) was to model the fracturing of the NaOH hexagonal shaped inclusions as a result of tensile liquid in the cavity (Figure 11). As a preamble, it is well known that geometrical singularities yield artificially increased stress in finite elements depending on the meshing. In addition, the real interface between the inclusion and the contained liquid is not as clear as in the geometrical model where the interface corresponds to a wall. Therefore, values of the simulated pressure must be carefully considered. The main purpose is to obtain tendencies that give us a better understanding of crack formation. As expected, the (negative) tensile pressure applied on the inner wall of the cavity (−200 MPa) yields a tensile state within the major part of the solid domain proved by the negative value of the simulated pressure (Figure 15, left). Like for the oblate spheroid model, the shape factor effect is observed as the pressure increase concentrates around the inclusion, reaching positive values along the cavity edges lying in the symmetry plane A, significantly higher than the applied inner pressure and indicating a compressive state in the plane induced by the predominant flattening of the cavity. The pressure reaches its highest values rather in the middle of

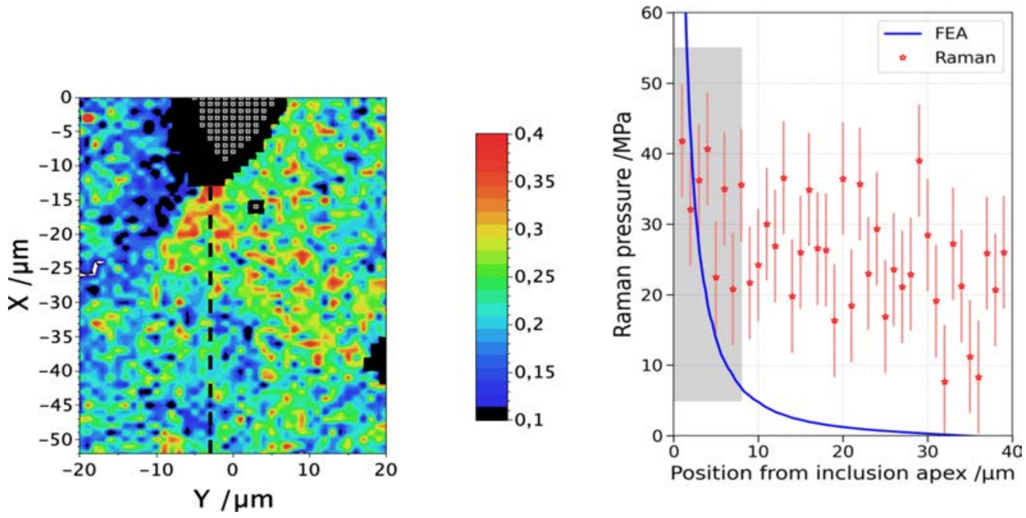

Figure 14. Left, Zooming in the southern area having the larger average wavenumber Raman shift (i.e., Figure 9). Right, Raman pressure (red stars) *vs* simulation (blue curve). The behavior close to the interface is highlighted as a gray area.

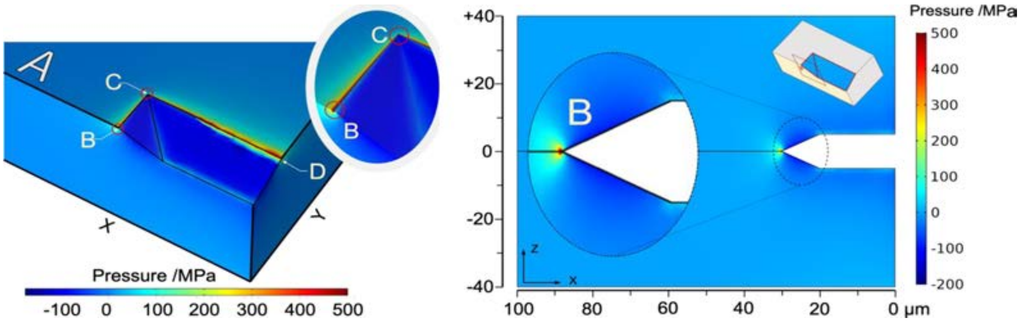

Figure 15. Pressure field showing (left) stress concentration along the longest edge lying in the symmetry plane XY (see Figure 5) near inclusion wall angles and (right) domains of negative/positive stress in the XZ symmetry plane.

the equatorial edges (e.g., points B and D) instead of the apex (e.g., point C) where the cracks form.

Focusing on the symmetry plane A (equatorial plane) that contains edges B-C-D of the inclusion, we observe that two principal stresses lie in plane A and that last one is perpendicular to the plane. This can be explained by the geometrical symmetry, quartz trigonal symmetry, and the orientation of the inclusion with respect to the crystallographic axes. The highest compressive stress is perpendicular to the equatorial plane aligned with crystallographic $c\rightarrow$ axis and is very concentrated along the cavity edges (Figure 16). The second compressive stress lies in the equatorial plane with lower magnitude (Figure 16b, compare the color scale with that of Figure 16a). The third principal stress also lies in the equatorial plane and shows negative values corresponding to tensile stress. It reaches its maximum magnitude around the apex C (Figure 16c, tensile stress). The tensile stress direction being along the line with the same origin and orientation as experimentally observed in the studied inclusions (Figure 11) confirms the possibility of crack formation along this line.

4. DISCUSSION

4.1. The Raman Pressure. Micro-Raman was here used to dynamically follow the internal pressure in a crystal hosting a variable pore tension. It is assumed that the applicability of the Grüneisen formalism allows us to translate the Raman shift into pressure. The anisotropy of monocrystalline quartz and the imperfections of the crystal lattice even under room conditions (see the Raman "irregularities" in Figure 7 left) limit this applicability. However, our study relies on the comparison of two datasets obtained at two different pore pressures, with all other parameters being constant. In addition, the shift is observed for two different Raman vibration modes, and it is very comparable. In that sense, the recorded Raman shift cannot be related to mechanisms other than lattice deformation and can be interpreted with confidence using the solid's linear elasticity.

Raman microspectrometry of silica minerals is commonly used to determine the pressure conditions of polymineralic assemblages containing various solid inclusions in minerals (e.g., refs[64−70]). The dominant compression mechanism is considered to be the reduction of (Si-O-Si) (e.g., ref.[71]). A similar Raman barometry is used for the $P-T$ conditions of the diamonds' source regions, based on determination of the internal pressure in olivine inclusions and the stresses in the surrounding diamond (e.g., refs.[72,73]). More recently, the Raman shifts of sapphires around a zircon inclusion were converted to hydrostatic pressure and deviatoric components of the stress tensor, combining micro-Raman and photoluminescence imaging techniques, linked by the piezospectroscopic effects on Raman and photoluminescence spectra.[74] The internal stress was highly concentrated at the tips of the zircon crystal, resulting in a compressive stress of several hundreds of MPa and leading to most inclusions in radial

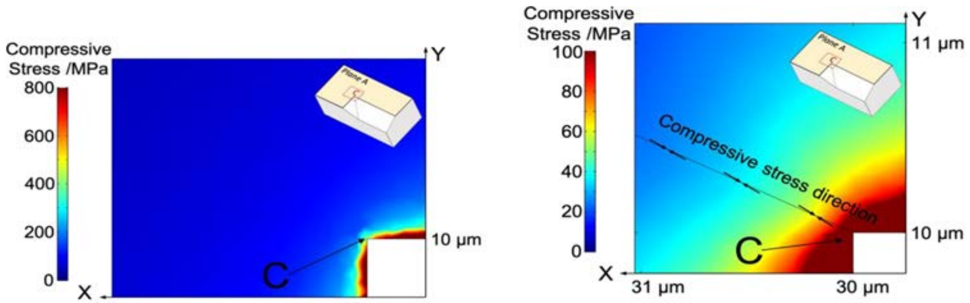

a) Compressive stress orthogonal to the map plane.

b) Compressive stress lying in the map plane and direction along the straight line of potential fracture.

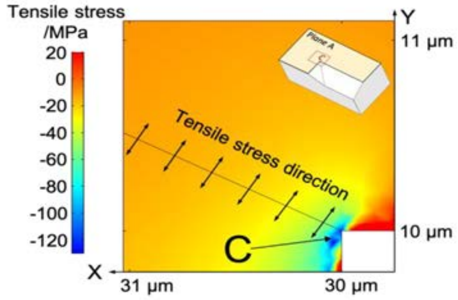

c) Tensile stress map and direction along the straight line of potential fracture.

Figure 16. Principal stress magnitude map near the corner of the symmetry plane XY (see Figure 5, plane noted A). (a) Principal compressive stress ($\sigma_\perp$) perpendicular to the plane. (b) Second principal compressive stress (σ_{II}) field near the corner of the symmetry plane XY (Figure 5, plane noted A). The double black arrows indicate the direction of σ_{II} along the line corresponding to the potential crack direction. (c) Principal tensile stress (σ_{T}) field near the corner of the symmetry plane XY (see Figure 9, plane noted A). The double black arrows indicate the direction of σ_{I} along the line corresponding to the potential crack direction. Note that negative/positive values indicate tensile/compressive stress.

cracks propagating in the host sapphire crystal from the apex of the hexagonal zircon. The present paper affords evidence that cracking can be invisible while leading to significant variation of the residual pressure. It could explain the growing observations in natural samples of a wide scattering of residual pressure sealed in inclusions (e.g., refs.[75−78]).

4.2. Crystal Host Stress Field. The comparison between simulation and Raman measurements is to some extent hindered by the heterogeneity displayed by the sample. When recording the spectroscopic signatures at RT, namely, the reference state without any external constraint, the data set showed significant variations of the Raman peaks across the whole map. Raman peaks showed a distribution into four quadrants, which remained almost unchanged whichever the fluid pressure (Figure 5). These measurements demonstrate that the host crystal is not the perfect, stress-free monocrystal assumed in the simulations. Experiments confirm the idea that the elastic deformations induced by the growing fluid pore tension retain and even magnify the initial imperfections. The Raman maps clearly show that the tension-driven shifts are amplified along the crystallographic axes. Therefore, both the Grüneisen formalism to convert Raman signatures into pressure and a direct comparison of such values to FEA simulations done through isotropic elastic theory can only approximately describe the complex mechanical behavior of quartz.

In spite of these limitations, the Raman measurements do retrieve features expected from elastic theory: (i) a compressive stress develops within the equatorial plane and (ii) the stress concentration is maximal in the vicinity of the cavity tip (Figure 14). Furthermore, the shape of the pore cavities plays a role in the stress field to build up a potentially complex 3D result (Figures 15 and 16). This complexity is certainly increased by the pre-existence, before installing any new constraints, of a certain degree of heterogeneity that is visible in the Raman maps at RT (Figure 7 left).

4.3. Stress Accumulation and Fracturing Threshold. It is difficult to be quantitative here; however, the stress generated around the water-bearing cavity appears moderate, especially compared to the observations of the damage (T_{H} variations, apex fractures) in the host quartz. One proposition for reconciling low stress and evidence of cracking is the role played by fatigue effects in the resistance of materials. Stresses that vary with time and in intensity are able to cause the rock failure while below the yield strength, and even in the linear elastic domain (e.g., refs.[5,79−81]). The best illustration is what is known as "reequilibration" in fluid inclusions studies, which is a modification of the inclusion shape and/or a fluid leakage because of the effective stress, namely, the pressure difference between host mineral stress and cavity-filling fluid pressure (e.g., refs[82−86]). One strong hypothesis, often claimed to infer various deep fluid conditions from fluid inclusions, is their isochoric behavior along the rock pathway throughout the Earth's crust (burial and/or uplift). To validate it, the resistance of quartz to differential stresses was measured on SFIs for internal under- or overpressure (respectively $P_{\mathrm{solid}} > P_{\mathrm{fluid}}$ or $P_{\mathrm{solid}} < P_{\mathrm{fluid}}$). Overpressure causes reequilibration from reaching 100 MPa.[82,85] Underpressure caused visible cracks from around 200 MPa, while reequilibration proceeded by dissolution−precipitation in the range of 100−200 MPa (e.g., ref.[83]). In a later study, cracking was observed when internal underpressure only exceeded 270 MPa.[85]

In our case, the amplitude of tensile stress in the inclusion, analogous to an underpressure stress, is either ∼200 MPa

(CsCl sample) or ∼140 MPa (NaOH sample). In spite of internal underpressure lower than [82−83]'s, we observed the formation of cracks with the lower differential stress. The simplest explanation for the difference is the effect of confining pressure, absent in our present study, while it is known to inhibit cracking.[85] An additional effect lies in the geometrical shape of the fluid inclusion, commonly spheroidal for natural inclusions. Our FEA modeling shows that the stress concentration at the tip of the inclusion reached a larger amplitude for the negative crystal shape (as displayed by the SFIs we used) than the spheroidal one. The geometry thus promotes the concentration of stress in the very limited area of the apex, which may facilitate crack initiation.

Furthermore, we can speculate a little more about the micromechanical mechanisms that underlie the development of cracks at low levels of tension. For instance, the microprestress theory[4] offers a comprehensive view of how capillary and disjoining pressures can drive the nucleation and growth of tensile microcracks in the complex pore network of an aging cement. In particular, hindered adsorption inside the nanoscale pores (1 to 10 molecular width and 0.3 to 3 nm) within hardened cement paste plays a pivotal role. It is appealing to hypothesize, for our experiments, the existence of tiny quantities of water present along the quartz dislocations comparable to the gel pores for cement. The liquid tension existing in the cavity might therefore spread over the nearby crystal lattice owing to minute water-bearing dislocations, propagating the tensile stress farther from the cavity and concentrating the constraints.

5. CONCLUSION AND PERSPECTIVES

The tension of water occluded in a crystalline cavity has a pore-scale micromechanical effect, as exemplified by the visible cracking for the NaOH sample, and the microthermometric features change (T_H increasing) for the CsCl sample. We demonstrated here that Raman spectroscopy is able to monitor in space and time the pressure in the quartz crystal around a fluid inclusion. The Raman maps revealed that the stress fields induced by the pore tension within the crystalline host rock are nonuniform and concentrated along the crystallographic orientations and, probably, crystal defects. The exact value of stress at these overstressed sites cannot be ascertained by the Raman technique because they may operate at a much smaller scale than the Raman scattering volume. The numerical-model simulated stress field and stress concentration match the measured 3D distribution of stress well and outline the role of geometry in terms of stress concentration in the region where fracturing was observed. On the contrary, the Raman estimates of how stress changes with distance from the inclusion do not match the elastic theory, showing that the crystal defects probably play a role in the stress distribution. Technically, micro-Raman associated with SFI microthermometry appears to be a powerful tool for deciphering the micromechanical mechanisms involved in complex field stress in rocks and porous media.

To summarize, our study demonstrates unambiguously that a permanent low stress as well as repeated cyclic stresses established in a crystal lattice by reducing the in-pore pressure in an occluded water-bearing cavity (related to capillary-type effects) is able to damage the hosting quartz despite its high resistance. The mechanical role pressurized pore fluids can play in weakening and embrittling rocks has long been known (e.g., refs.[87,88]), and this paper is a first step in envisioning the role of tensile pore fluids. Furthermore, this result poses the question of the mid/long-term safety of geological storage (CO_2, nuclear wastes, energy) wherever the geological formations are subjected to drying operations that make it possible to install liquid tension in large masses of unsaturated hydrosystems. In particular, the use of clayey formations to guarantee the confinement of the nuclear species owing to this impermeable barrier must be questioned if the consequent tension of tunnel ventilation was able to enhance permeability in the massif by creating fissures. In the same way, the integrity of the caprocks in CO_2 storage is a crucial property that prevents any leakage from occurring. However, the injection of supercritical CO_2 severely dries out the formation, especially at the highest part where the CO_2 bubble accumulates at the very contact with the caprock, establishing the right conditions for tension-driven processes.

During the course of the study, the initiation of microcracking and brittle failure was also discussed in association with the water distribution in rock. This aspect is of great significance in natural systems, beyond the question of storage safety. At high pressure and temperature, where deformation proceeds mainly as a result of temperature-dependent viscous creep processes (dislocation- or diffusion creep), fracturing is still present. These brittle precursors promote grain-size reduction and therefore the fluid flow and chemical reactions that activate water corrosion.[89−91] High fluid pressures, up to confining pressure values, are necessary to open cracks, but the mechanisms are not well understood, even if we know that the physical state of the water present in mineral assemblages with very low porosity is often involved as a triggering mechanism.[92,93] This study demonstrates that reducing fluid pressure also induces cracking mechanisms rooted at the small scale, even if the generality *versus* specificity of such mechanisms in the various pressure contexts is still to be explored.

■ AUTHOR INFORMATION

Corresponding Author

Lionel Mercury − *ISTO, UMR 7327, Univ. Orléans, CNRS, BRGM, Orléans F-45071, France;* orcid.org/0000-0002-3825-663X; Email: lionel.mercury@univ-orleans.fr

Authors

Emmanuel De Bilbao − *CEMHTI, UPR3079 CNRS, Univ. Orléans, Orléans F-45071, France*
Patrick Simon − *CEMHTI, UPR3079 CNRS, Univ. Orléans, Orléans F-45071, France*
Hugues Raimbourg − *ISTO, UMR 7327, Univ. Orléans, CNRS, BRGM, Orléans F-45071, France*
Isabelle Bergonzi − *ISTO, UMR 7327, Univ. Orléans, CNRS, BRGM, Orléans F-45071, France*
Claudie Hulin − *ISTO, UMR 7327, Univ. Orléans, CNRS, BRGM, Orléans F-45071, France*
Aurélien Canizarès − *CEMHTI, UPR3079 CNRS, Univ. Orléans, Orléans F-45071, France*
Kirill I. Shmulovich − *Institute of Experimental Mineralogy, Russian Academy of Science, Chernogolovka 142432, Russia*

Complete contact information is available at:
https://pubs.acs.org/10.1021/acsearthspacechem.0c00224

Notes

The authors declare no competing financial interest.

■ ACKNOWLEDGMENTS

This work has received financial support from the French Agency for Research (Agence Nationale de la Recherche), through the grant CONGE BLAN-610-01, the Equipex Planex ANR-11-EQPX-36 and the Labex Voltaire ANR-10-LABX-100-01. The authors are indebted to R. Bodnar, X. Zhong, and a third reviewer for their positive and detailed criticisms which improved the initial manuscript. The English language was also improved by K. Tkaczyk, from McMillan translations. The authors warmly thank Dr. C. Meng for sharing and adapting his scripts for Eshelby theory-based calculations.

■ REFERENCES

(1) Eppes, M.-C.; Keanini, R. Mechanical weathering and rock erosion by climate-dependent subcritical cracking. *Rev. Geophys.* **2017**, *55*, 470−508.

(2) Anderson, S. P. Breaking it down: mechanical processes in the weathering engine. *Elements* **2019**, *15*, 247−252.

(3) Van Eeckhout, E. M. The Mechanisms of Strength Reduction due to Moisture in Coal Mine Shales. *Int. J. Rock Mech. Min. Sci. Geomech. Abstr.* **1976**, *13*, 61−67.

(4) Bažant, Z. P.; Hauggaard, A. E.; Baweja, S.; Ulm, F.-J. Microprestress-solidification theory for concrete creep. I: aging and drying effects. *J. Eng. Mech.* **1997**, *123*, 1188−1194.

(5) Atkinson, B. K. Subcritical crack growth in geological materials. *J. Geophys. Res.* **1984**, *89*, 4077−4114.

(6) Scherer, G. W. Crack-tip stress in gels. *J. Non-Cryst. Solids* **1992**, *144*, 210−216.

(7) Dufresne, E. R.; Corwin, E. I.; Greenblatt, N. A.; Ashmore, J.; Wang, D. Y.; Dinsmore, A. D.; Cheng, J. X.; Xie, X. S.; Hutchinson, J. W.; Weitz, D. A. Flow and fracture in drying nanoparticle suspensions. *Phys. Rev. Lett.* **2003**, *91*, 224501. 4 pages

(8) Lee, W. P.; Routh, A. F. Why do drying films crack? *Langmuir* **2004**, *20*, 9885−9888.

(9) Bažant, Z. P. Thermodynamics of hindered adsorption and its implications for hardened cement paste and concrete. *Cement Concrete Res.* **1972**, *2*, 1−16.

(10) Bažant, Z. P.; Wu, S. T. Creep and shrinkage law of concrete at variable humidity. *J. Eng. Mech. Div. ASCE* **1974**, *18*, 1183−1120.

(11) Coussy, O.; Dangla, P.; Lassabatère, T.; Baroghel-Bouny, V. The equivalent pore pressure and the swelling and shrinkage of cement-based materials. *Mater. Struct.* **2004**, *37*, 15−20.

(12) Lagier, F.; Jourdain, X.; De Sa, C.; Benboudjema, F.; Colliat, J. B. Numerical strategies for prediction of drying cracks in heterogeneous materials: Comparison upon experimental results. *Eng. Struct.* **2011**, *33*, 920−931.

(13) Li, Y.; Li, J. Capillary tension theory for prediction of early autogenous shrinkage of self-consolidating concrete. *Construct. Build. Mater.* **2014**, *53*, 511−516.

(14) Scherer, G. W. Drying, Shrinkage, and Cracking of Cementitious Materials. *Transp. Porous Media* **2015**, *110*, 311−331.

(15) Charlier, R.; Collin, F.; Pardoen, B.; Talandier, J.; Radu, J. P.; Gerard, P. An unsaturated hydro-mechanical modelling of two in-situ experiments in Callovo-Oxfordian argillite. *Eng. Geol.* **2013**, *165*, 46−63.

(16) Armand, G.; Noiret, A.; Zghondi, J.; Seyedi, D. M. Short- and long-term behaviors of drifts in the Callovo-Oxfordian claystone at the Meuse/Haute-Marne Underground research Laboratory. *J. Rock Mech. Geotech. Eng.* **2013**, *5*, 221−230.

(17) Vinsot, A.; Leveau, F.; Bouchet, A.; Arnould, A. Oxidation front and oxygen transfer in the fractured zone surrounding the Meuse/Haute-Marne URL drifts in the Callovian−Oxfordian argillaceous rock. In *Clays in Natural and Engineered Barriers for Radioactive Waste Confinement* (Norris, S.; Bruno, J.; Cathelineau, M.; Delage, P.; Fairhurst, C.; Gaucher, E.C.; Höhn, E. H.; Kalinichev, A.; Lalieux, P.; Sellin, P., editors). Geological Society, London, Special Publications 2014, *400*, 207−220.

(18) Vinsot, A.; Linard, Y.; Lundy, M.; Necib, S.; Wechner, S. Insights on desaturation processes based on the chemistry of seepage water from boreholes in the Callovo-Oxfordian argillaceous rock. *Procedia Earth Planet. Sci.* **2013**, *7*, 871−874.

(19) Pardoen, B.; Talandier, J.; Colin, F. Permeability evolution and water transfer in the excavation damaged zone of a ventilated gallery. *Int. J. Rock Mech. Mining Sci.* **2016**, *85*, 192−208.

(20) Vinsot, A.; Lundy, M.; Linard, Y. O_2 Consumption and CO_2 Production at Callovian-oxfordian Rock Surfaces. *Procedia Earth Planet. Sci.* **2017**, *17*, 562−565.

(21) Osselin, F.; Fen-Chong, T.; Fabbri, A.; Lassin, A.; Pereira, J.-M.; Dangla, P. Dependence on injection temperature and on aquifer's petrophysical properties of the local stress applying on the pore wall of a crystallized pore in the context of CO_2 storage in deep saline aquifers. *Eur. Phys. J. Appl. Phys.* **2013**, *64*, 21101 10 pages.

(22) Peysson, Y.; André, L.; Azaroual, M. Well injectivity during CO_2 storage operations in deep saline aquifers− Part 1: Experimental investigation of drying effects, salt precipitation and capillary forces. *Int. J. Greenhouse Gas Control* **2014**, *22*, 291−300.

(23) Ott, H.; Andrew, M.; Snippe, J.; Blunt, M. J. Microscale solute transport and precipitation in complex rock during drying. *Geophys. Res. Lett.* **2015**, *41*, 8369−8376.

(24) Turuntaev, S.; Merchaeva, O.; Zenchenko, E. Formation fracturing by pore pressure drop (laboratory study). In *ISRM International Conference for Effective and Sustainable Hydraulic Fracturing*. International Society for Rock Mechanics and Rock Engineering, 2013, Chap. *51*, 993−1011. DOI: 10.5772/56303.

(25) David, C.; Dautriat, J.; Sarout, J.; Delle Piane, C.; Menendez, B.; Macault, R.; Bertauld, D. Mechanical instability induced by water weakening in laboratory fluid injection tests. *J. Geophys. Res. Solid Earth* **2015**, *120*, 4171−4188.

(26) Røyne, A.; Meakin, P.; Malthe-Sørenssen, A.; Jamtveit, B.; Dysthe, D. K. Crack propagation driven by crystal growth. *EPL* **2011**, *96*, 24003. 6 pages

(27) Green, J. L.; Durben, D. J.; Wolf, G. H.; Angell, C. A. Water and solutions at negative pressure: Raman spectroscopic study to −80 Megapascals. *Science* **1990**, *249*, 649−652.

(28) Zheng, Q.; Durben, D. J.; Wolf, G. H.; Angell, C. A. Liquids at large negative pressures: water at the homogeneous nucleation limit. *Science* **1991**, *254*, 829−832.

(29) Alvarenga, A. D.; Grimsditch, M.; Bodnar, R. J. Elastic properties of water under negative pressures. *J. Chem. Phys.* **1993**, *98*, 8392−8396.

(30) Shmulovich, K.; Mercury, L.; Thiéry, R.; Ramboz, C.; El Mekki, M. Experimental superheating of water and aqueous solutions. *Geochim. Cosmochim. Acta* **2009**, *73*, 2457−2470.

(31) Fall, A.; Rimstidt, J. D.; Bodnar, R. J. The effect of fluid inclusion size on determination of homogenization temperature and density of liquid-rich aqueous inclusions. *Am. Mineral.* **2009**, *94*, 1569−1579.

(32) Holmes, H. F.; Mesmer, R. E. Thermodynamic properties of aqueous solutions of the alkali metal chlorides to 250°C. *J. Phys. Chem.* **1983**, *87*, 1242−1255.

(33) Roedder, E. Metastable superheated ice in liquid-water inclusions under high negative pressure. *Science* **1967**, *155*, 1413−1417.

(34) Qiu, C.; Krüger, Y.; Wilke, M.; Marti, D.; Rička, J.; Frenz, M. Exploration of the phase diagram of liquid water in the low temperature metastable region using synthetic fluid inclusion. *Phys. Chem. Chem. Phys.* **2016**, *18*, 28227−28241.

(35) Henderson, S. J.; Speedy, R. J. Melting Temperature of Ice at Positive and Negative Pressures. *J. Phys. Chem.* **1987**, *91*, 3069−3072.

(36) Barrow, M. S.; Williams, P. R.; Chan, H.-H.; Dore, J. C.; Bellissent-Funel, M.-C. Studies of cavitation and ice nucleation in 'doubly-metastable' water: time-lapse photography and neutron diffraction. *Phys. Chem. Chem. Phys.* **2012**, *14*, 13255−13261.

(37) Wagner, W.; Pruss, A. The IAPWS Formulation 1995 for the Thermodynamic Properties of Ordinary Water Substance for General and Scientific Use. *J. Phys. Chem. Ref. Data* **2002**, *31*, 387−535.

(38) Marti, D.; Krüger, Y.; Fleitmann, D.; Frenz, M.; Ricka, J. The effect of surface tension on liquid-gas equilibria in isochoric systems and its application to fluid inclusions. *Fluid Phase Equilib.* **2012**, *314*, 13−21.

(39) Mercury, L.; Shmulovich, K. I.; Bergonzi, I.; Canizares, A.; Simon, P. Growing negative pressure in fluid inclusions: Raman monitoring of solvent-pulling effect. *J. Phys. Chem. C* **2016**, *120*, 7697−7704.

(40) Parlinsky, K. *Ab initio* determination of anharmonic phonon peaks. *Phys. Rev. B* **2018**, *98*, No. 054305.

(41) Le Parc, R.; Buixaderas, E.; Levelut, C.; Hermet, P.; Pereira, A. S.; Cambon, O.; Roiland, C.; Simon, P.; Haines, J. Ultrastable phonon frequencies in α-quartz-type BPO4 at high temperature. *Appl. Phys. Lett.* **2019**, *115*, No. 141902.

(42) Schmidt, C.; Ziemann, M. A. In-situ Raman spectroscopy of quartz: A pressure sensor for hydrothermal diamond-anvil cell experiments at elevated temperatures. *Am. Mineral.* **2000**, *85*, 1725−1734.

(43) Gregora, I.; Magneron, N.; Simon, P.; Luspin, Y.; Raimboux, N.; Philippot, E. Raman Study of AlPO4 Berlinite at the Alpha-Beta Transition. *J. Phys. Condens. Matter* **2003**, *15*, 4487−4501.

(44) Healy, D. Elastic field in 3D due to a spheroidal inclusion: MATLAB code for Eshelby's solution. *Comput. Geosci.* **2009**, *35*, 2170−2173.

(45) Eshelby, J. D.; Peierls, R. E. The determination of the elastic field of an ellipsoidal inclusion, and related problems. *Proc. R. Soc. Lond. A* **1957**, *241*, 376−396.

(46) Mura, T.; Jasiuk, I.; Tsuchida, B. The stress field of a sliding inclusion. *Int. J. Solids Struct.* **1985**, *21*, 1165−1179.

(47) Mura, T. *Micromechanics of Defects in Solids*. Springer Netherlands. 1987.

(48) Lee, M.; Jasiuk, I.; Tsuchida, E. The Sliding Circular Inclusion in an Elastic Half-Plane. *J. Appl. Mech.* **1992**, *59*, S57−S64.

(49) Pukánszky, B.; Vörös, G. Stress distribution around inclusions, interaction, and mechanical properties of particulate-filled composites. *Polym. Compos.* **1996**, *17*, 384−392.

(50) Fialko, Y.; Khazan, Y.; Simons, M. Deformation due to a pressurized horizontal circular crack in an elastic half-space, with applications to volcano geodesy. *Geophys. J. Int.* **2001**, *146*, 181−190.

(51) Meng, C. Esh3D, an Analytical and Numerical Hybrid Code for Full Space and Half-Space Eshelby's Inclusion Problems. *Earth Space Sci.* **2019**, *6*, 505−514.

(52) Meng, C. Extending Esh3D Code to Solve Interacting Eshelby's Inhomogeneity Problems. *Earth Space Sci.* **2019**, *6*, 1569−1577.

(53) Meng, C.; Heltsley, W.; Pollard, D. Evaluation of the Eshelby Solution for the Ellipsoidal Inclusion and Heterogeneity. *Comput. Geosci.* **2012**, *40*, 40−48.

(54) Zhong, X.; Dabrowski, M.; Jamtveit, B. Analytical solution for the stress field in elastic half-space with a spherical pressurized cavity or inclusion containing eigenstrain. *Geophys. J. Int.* **2019**, *216*, 1100−1115.

(55) Zienkievicz, O.C.; Taylor, R.L. *The finite element method for solid and structural mechanics*. Elsevier Butterworth-Heinemann, 2005, 632.

(56) Heyliger, P.; Ledbetter, H.; Kim, S. Elastic constants of natural quartz. *J. Acoust. Soc. Am.* **2003**, *114*, 644−650.

(57) Calderon, E.; Gauthier, M.; Decremps, F.; Hamel, G.; Syfosse, G.; Polian, A. Complete determination of the elastic moduli of α-quartz under hydrostatic pressure up to 1 GPa: an ultrasonic study. *J. Phys.: Condens. Matter* **2007**, *19*, No. 436228.

(58) Takahashi, M.; Izawa, E.; Etou, J.; Ohtani, T. Kinetic characteristic of bubble nucleation in superheated water using fluid inclusions. *J. Phys. Soc. Jpn.* **2002**, *71*, 2174−2177.

(59) Bouzid, M.; Mercury, L.; Lassin, A.; Matray, J.-M. Salt precipitation and trapped liquid cavitation in micrometric capillary tubes. *J. Colloid Interf. Sci.* **2011**, *360*, 768−776.

(60) El Mekki, M.; Ramboz, C.; Lenain, J.-F.; Caupin, F. A coherent picture of water at extreme negative pressure. *Nat. Phys.* **2013**, *9*, 38−41.

(61) Bodnar, R. J.; Bethke, P. M. Systematics of stretching of fluid inclusions. I. Fluorite and sphalerite at 1 atmosphere confining pressure. *Economic Geol.* **1984**, *79*, 141−161.

(62) Anastassakis, E.; Pinczuk, A.; Burstein, E.; Pollak, F. H.; Cardona, M. Effect of static uniaxial stress on the Raman spectrum of silicon. *Solid State Commun.* **1970**, *8*, 133−138.

(63) Briggs, R. J.; Ramdas, A. K. Piezospectroscopy of the Raman spectrum of -quartz. *Phys. Rev. B* **1977**, *16*, 3815−3826.

(64) Hemley, R.J. Pressure dependence of Raman spectra of SiO_2 polymorphs: -quartz, coesite and stishovite. In *High pressure research in mineral physics* (Manghani, M.H; Syono, Y. Eds), 1987, 347−359. American Geophysical Union, Washington, D.C.

(65) Ye, K.; Liou, J.-B.; Vong, B.; Maruyama, S. Overpressures induced by coesite-quartz transition in zircon. *Am. Mineral.* **2001**, *86*, 1151−1155.

(66) Korsakov, A. V.; Hutsebaut, D.; Theunissen, K.; Vandenabeele, P.; Stepanov, A. S. Raman mapping of coesite inclusions in garnet from the Kokchetav Massif (Northern Kazakhstan). *Spectrochim. Acta Part A* **2007**, *68*, 1046−1052.

(67) Ashley, K.; Caddick, M.; Steele-MacInnis, M.; Bodnar, R. J.; Dragovic, B. Geothermobarometric history of subduction recorded by quartz inclusions in garnet. *Geochem. Geophys. Geosyst.* **2014**, *15*, 350−360.

(68) Ashley, K. T.; Darling, R. S.; Bodnar, R. J.; Law, R. D. Significance of "stretched" mineral inclusions for reconstructing P-T exhumation history. *Contrib. Mineral. Petrol.* **2015**, *169*, 9.

(69) Ashley, K. T.; Steele-MacInnis, M.; Bodnar, R. J.; Darling, R. S. Quartz-in-garnet inclusion barometry under fire: Reducing uncertainty from model estimates. *Geology* **2016**, *44*, 699−702.

(70) Cisneros, M.; Ashley, K. T.; Bodnar, R. J. Evaluation and application of the quartz-inclusions in epidote mineral barometer. *Am. Mineral.* **2020**, *105*, 1140−1151.

(71) Parkinson, C. D.; Katayama, I. Present-day ultrahigh-pressure conditions of coesite inclusions in zircon and garnet: Evidence from laser Raman micro-spectroscopy. *Geology* **1999**, *27*, 979−982.

(72) Izraeli, E. S.; Harris, J. W.; Navon, O. Raman barometry of diamond formation. *Earth Planet. Sci. Lett.* **1999**, *173*, 351−360.

(73) Nasdala, L.; Hofmeister, W.; Harris, J. W.; Glinnemann, J. Growth zoning and strain patterns inside diamond crystals as revealed by Raman maps. *Am. Mineral.* **2005**, *90*, 745−748.

(74) Noguchi, N.; Abduriyim, A.; Shimizu, I.; Kamegata, N.; Odake, S.; Kagi, H. Imaging of internal stress around a mineral inclusion in a sapphire crystal: application of micro-Raman and photoluminescence spectroscopy. *J. Raman Spectrosc.* **2013**, *44*, 147−154.

(75) Enami, M.; Nishiyama, T.; Mouri, T. Laser Raman microspectrometry of metamorphic quartz: A simple method for comparison of metamorphic pressures. *Am. Mineral.* **2007**, *92*, 1303−1315.

(76) Kouketsu, Y.; Nishiyama, T.; Ikeda, T.; Eniami, M. Evaluation of residual pressure in an inclusion − host system using negative frequency shift of quartz Raman spectra. *Am. Mineral.* **2014**, *99*, 433−442.

(77) Taguchi, T.; Enami, M.; Kouketsu, Y. Metamorphic record of the Asemi-gawa eclogite unit in the Sanbagawa belt, southwest Japan: Constraints from inclusions study in garnet porphyroblasts. *J. Metamorph. Geol.* **2019**, *37*, 181−201.

(78) Zhong, X.; Andersen, N. H.; Dabrowski, M.; Jamtveit, B. Zircon and quartz inclusions in garnet used for complementary Raman thermobarometry: application to the Holsnøy eclogite, Bergen Arcs, Western Norway. *Contrib. Mineral. Petrol.* **2019**, *174*, 50−66.

(79) Darot, M.; Gueguen, Y. Slow crack growth in minerals and rocks: theory and experiments. *Pure Appl. Geophys.* **1986**, *124*, 677−692.

(80) Mallet, C.; Fortin, J.; Gueguen, Y.; Bouyer, F. Role of the pore fluid in crack propagation in glass. *Mech. Time-Depend. Mater.* **2015**, *19*, 117−133.

(81) Ougier-Simonin, A.; Zhu, W. Effect of the pore pressure buildup on slowness of rupture propagation. *J. Geophys. Res.* **2015**, *120*, 7966−7985.

(82) Sterner, S. M.; Bodnar, R. J. Synthetic fluid inclusions - VII. Re-equilibration of fluid inclusions in quartz during laboratory-simulated metamorphic burial and uplift. *J. Metamorph. Geol.* **1989**, *7*, 243−260.

(83) Vityk, M. O.; Bodnar, R. J.; Schmidt, C. S. Fluid inclusions as tectonothermobarometers: Relation between pressure-temperature history and reequilibration morphology during crustal thickening. *Geology* **1994**, *22*, 731−734.

(84) Vityk, M. O.; Bodnar, R. J. Do fluid inclusions in high-grade metamorphic terranes preserve peak metamorphic density during retrograde decompression? *Am. Mineral.* **1995a**, *80*, 641−644.

(85) Vityk, M. O.; Bodnar, R. J. Textural evolution of synthetic fluid inclusions in quartz during reequilibration, with applications to tectonic reconstruction. *Contrib. Mineral. Petrol.* **1995b**, *121*, 309−323.

(86) Raimbourg, H.; Famin, V.; Palazzin, G.; Mayoux, M.; Jolivet, L.; Ramboz, C.; Yamaguchi, A. Fluid properties and dynamics along the seismogenic plate interface. *Geosphere* **2018**, *14*, 469−491.

(87) Paterson, M.S. *Experimental rock deformation − The brittle field*, Springer Verlag, Berlin, 1978.

(88) Bruno, M. S.; Nakagawa, F. M. Pore pressure influence on tensile fracture propagation in sedimentary rock. *Int. J. Rock Mech. Min. Sci. Geomech. Abstr.* **1991**, *28*, 261−273.

(89) Austrheim, H. Eclogitization of lower crustal granulites by fluid migration through shear zones. *Earth Planet. Sci. Lett.* **1987**, *81*, 221−232.

(90) Goncalves, P.; Poilvet, J.-C.; Oliot, E.; Trap, P.; Marquer, D. How does shear zone nucleate? An example from the Suretta nappe (Swiss Eastern Alps). *J. Struct. Geol.* **2016**, *86*, 166−180.

(91) Leydier, T.; Goncalves, P.; Lanari, P.; Oliot, E. On the petrology of brittle precursors of shear zones − An expression of concomitant brittle deformation and fluid−rock interactions in the 'ductile' continental crust? *J. Metamorph. Geol.* **2019**, *37*, 1129−1149.

(92) Den Brok, B. Effect of microcracking on pressure-solution strain rate: The Gratz grain-boundary model. *Geology* **1998**, *26*, 915−918.

(93) Nakashima, S.; Matayoshi, H.; Yuko, T.; Michibayashi, K.; Masuda, T.; Kuroki, N.; Yamagashi, H.; Ito, Y.; Nakamura, A. Infrared microspectroscopy analysis of water distribution in deformed and metamorphosed rocks. *Tectonophysics* **1995**, *245*, 263−276.

https://dx.doi.org/10.1021/acsearthspacechem.0c00224